Biocompatible and pH-Sensitive PLGA Encapsulated MnO Nanocrystals for Molecular and Cellular MRI

Margaret F. Bennewitz,[†] Tricia L. Lobo,[§] Michael K. Nkansah,[†] Gözde Ulas,[‡] Gary W. Brudvig,[‡] and Erik M. Shapiro[†,§,*]

[†]Department of Biomedical Engineering, Yale University, 300 Cedar Street, New Haven, Connecticut 06520, United States, [‡]Department of Chemistry, Yale University, 225 Prospect Street, New Haven, Connecticut 06520, United States, and [§]Magnetic Resonance Research Center Department of Diagnostic Radiology, Yale University School of Medicine, 300 Cedar Street, New Haven, Connecticut 06520, United States

ABSTRACT Inorganic manganese-based particles are becoming attractive for molecular and cellular imaging, due to their ability to provide bright contrast on MRI, as opposed to the dark contrast generated from iron-based particles. Using a single emulsion technique, we have successfully fabricated pH-sensitive poly(lactic-*co*-glycolic acid) (PLGA)-encapsulated manganese oxide (MnO) nanocrystals. Two classes of particles were fabricated at ~140 nm and 1.7 μm and incorporated 15 to 20 nm MnO nanocrystals with high encapsulation efficiencies. Intact particles at physiological pH cause little contrast in MRI, but following endocytosis into low pH compartments within the cells, the particles erode and MnO dissolves to release Mn^{2+}. This causes the cells to appear bright on MR images. The magnitude of the change in MRI properties is as high as 35-fold, making it the most dynamic "smart" MRI contrast agent yet reported. Possible applications of these MnO particles include slow release Mn^{2+}, tumor targeting, and confirmation of cell uptake.

KEYWORDS: MRI · manganese · cells · contrast agents · PLGA · nanoparticles · microparticles

The manganese ion (Mn^{2+}) has been a useful MRI contrast agent since the first description of its use in 1979 to delineate cardiac infarction in dogs.[1] Mn^{2+} is almost always delivered as a water-soluble manganese salt and has been delivered by a myriad of routes, including intravenous (iv),[2] intraparenchymal (ip),[3] or subcutaneous injection,[4] directly into the brain[5] or nose[6] or peripherally.[7] In living systems, water-soluble Mn^{2+} is handled similarly to Ca^{2+} and can enter cells *via* voltage-gated calcium channels.[8] Internalized Mn^{2+} can furthermore travel down active neurons and leap neuronal junctions.[6] These are the basic principles behind dynamic activity induced manganese (AIM) imaging[9] and manganese-enhanced MRI (MEMRI).[10]

Recently, interest has gained in inorganic manganese-based particles for molecular and cellular MRI.[11−16] Particle cores have taken the form of manganese oxides (MnO, Mn_3O_4, and MnO_2) and manganese carbonate ($MnCO_3$). These cores are insoluble in water, and without particle coatings, cores precipitate out of solution. In most cases, particles have very low molar relaxivities, < 0.5 mM^{-1} s^{-1}, owing to the lack of water contact with the manganese atoms, and therefore cause little signal enhancement in MRI.

Inorganic manganese-based particles have been used as both a targeted nanoparticle (NP) for molecular MRI[13] as well as an MRI-based cell tracking T_1 agent.[12] In both cases following administration of the NPs, either by iv injection[13] or by direct *in vitro* cellular incubation,[12] bright contrast was observed by T_1-weighted MRI. These results were interpreted as T_1 contrast directly attributed to intact manganese particles.

While manganese oxides and carbonates are insoluble in water, they will dissolve slowly in acidic conditions.[11] It is well-established that, upon internalization into cells, NPs and microparticles (MPs) are shuttled to low pH compartments within the cells.[17,18] Thus, another interpretation of the above results is that bright contrast in manganese particle-labeled cells is due to the evolved Mn^{2+}, which has an r_1 molar relaxivity of 7 mM^{-1} s^{-1}, as a result of slow dissolution within low pH endosomes. This is supported by recent studies on dissolution of inorganic manganese cores in low pH buffers giving rise to bright contrast on MR images.[11] Indeed, if this is the case, then delivery of manganese particles to specific cell populations could serve as a slow release reservoir *in vivo*. Furthermore, one can envision the use of these kinds of particles to verify endocytosis of delivered particles, as in a targeted MRI experiment, or whether particles simply remain extracellular. Lastly, these kinds of particles might prove useful

* Address correspondence to erik.shapiro@yale.edu.

Received for review August 10, 2010 and accepted April 15, 2011.

Published online April 15, 2011
10.1021/nn1019779

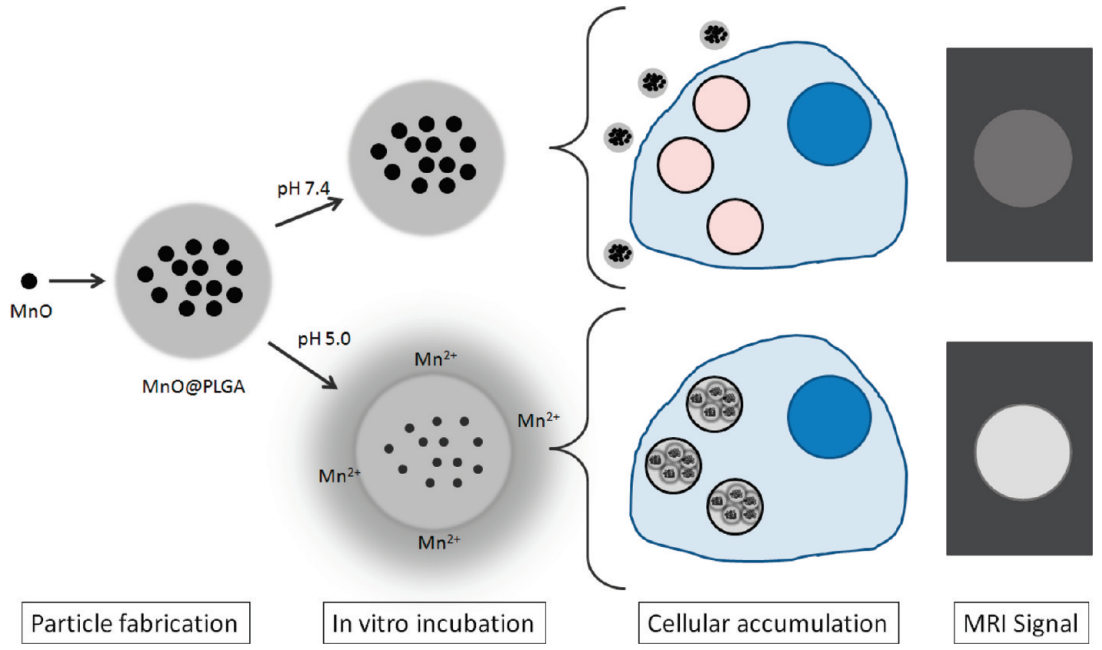

Figure 1. Conceptual schematic of MnO encapsulation in PLGA, followed by release of Mn^{2+} in low pH. This results in increased r_1, leading to enhancement in MRI. The *in vitro* experiment is a mimic of lysosomal uptake of particles by cells.

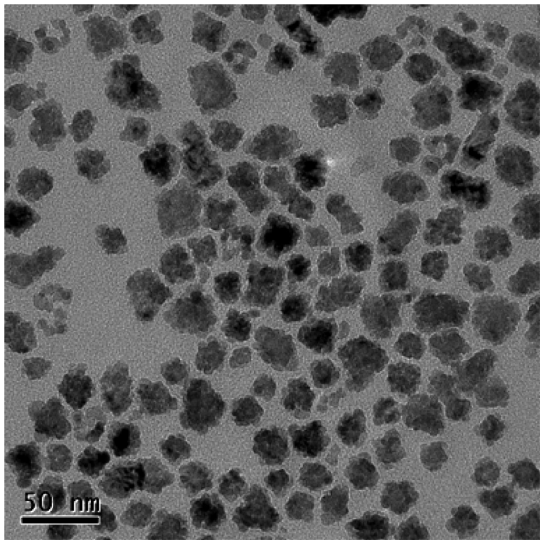

Figure 2. TEM of MnO nanocrystals. Sizes are approximately 15–20 nm.

in reporting on the location of tumors by way of their slightly acidic pH, resulting in evolved Mn^{2+} and bright contrast in MR images.

Here we propose a novel paradigm for utilizing MnO nanocrystals for molecular and cellular MRI by encapsulating high quantities of MnO within poly(lactic-*co*-glycolic acid) (PLGA) NPs and MPs (Figure 1). PLGA is a well-described and characterized polymer long used for particle-based drug delivery due to its established safety, biocompatibility, and approval by the FDA. On the basis of previous success of magnetic cell labeling *in vitro* with 150 nm dextran-coated iron oxide nanoparticles[19] as well as both *in vitro*[20] and *in vivo*[21] with inert 1.63 μm sized iron oxide particles, we aimed to produce PLGA-encapsulated MnO particles at these two size regimes. We demonstrate how these particles have very low r_1 molar relaxivities as intact particles and elicit high r_1 molar relaxivities upon dissolution in acidic media.

Fifteen to 20 nm MnO nanocrystals were fabricated by thermal decomposition of manganese(II) acetylacetonate (MnACAC) in benzyl ether and oleic acid at 300 °C under nitrogen for 2 h, similar to the established protocol of ref 22. Upon cooling, the resulting MnO nanocrystals were precipitated in hexane and ethanol, collected by centrifugation, and dried overnight in a vacuum oven. Transmission electron microscopy (TEM) of the MnO cores shows 15–20 nm aggregates of several 5–10 nm cores (Figure 2). Crystal structure and molecular identity of the synthesized MnO nanocrystals were confirmed with powder X-ray diffraction (Supporting Figure S1).

Next, PLGA-encapsulated MnO nanocrystals were fabricated with a single emulsion process, using methylene chloride as the organic solvent and polyvinyl alcohol (PVA) as the stabilizer. Particles were fabricated using either 50 or 100% w/w MnO/PLGA. Control particles were fabricated without MnO. Sonication and homogenization disruption techniques were utilized to form the primary emulsions for NPs and MPs, respectively. Following hardening, particles were washed with deionized water and dried on a lyophilizer. Fluorescent MnO NPs and MPs were fabricated by adding coumarin-6, a green fluorescent dye, at the same time as the MnO nanocrystals were added to the polymer/solvent mixture.

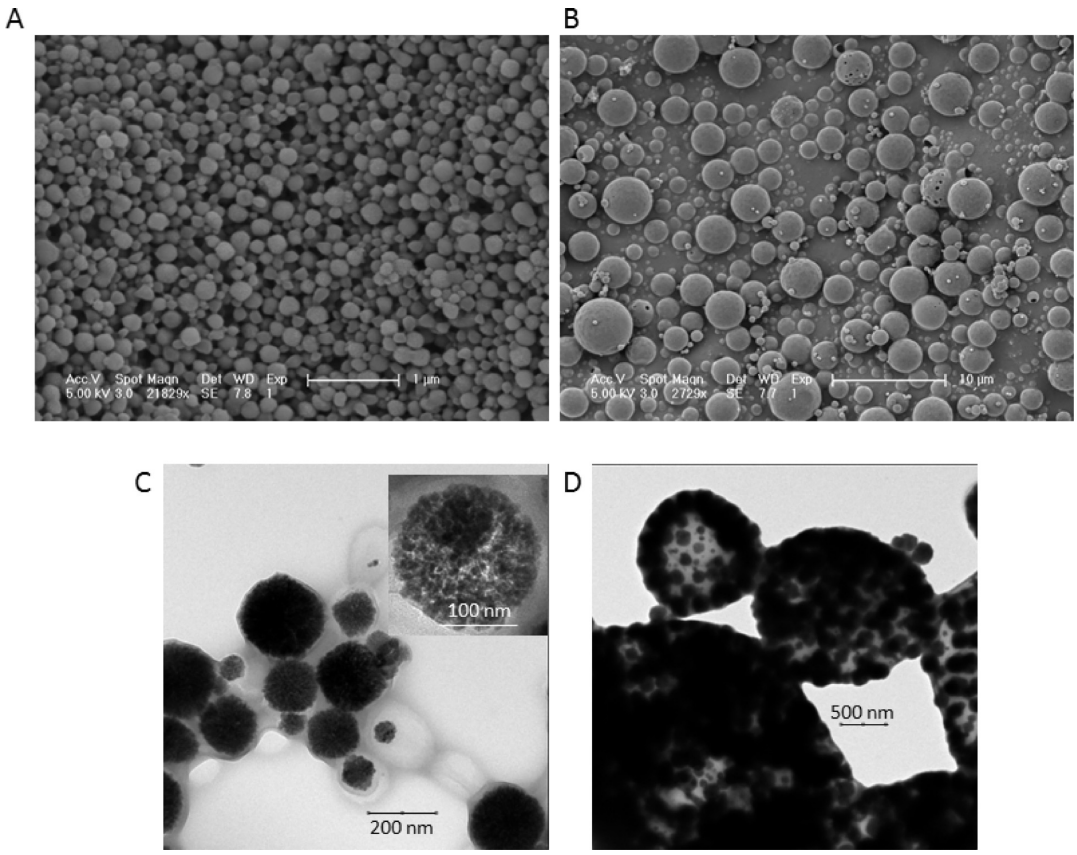

Figure 3. SEM (A,B) and TEM (C,D) of NPs and MPs. (A) NPs and (B) MPs had average sizes of approximately 140 nm and 1.7 μm, respectively. The scale bar for NPs is 1 μm and MPs is 10 μm. Note how the particles show a regular, spherical morphology. (C) TEM of NPs with the inset showing nanocrystals distributed throughout a single particle. (D) TEM of MPs also showing nanocrystals disbursed throughout.

TABLE 1. Weight Percents and Encapsulation Efficiencies for MnO NPs and MPs

particle type	wt % (MnO)	EE%
50% MnO NP	52.5	157.5
100% MnO NP	62.5	125
50% MnO MP	35	105
100% MnO MP	46.5	93

Size of the particles was assessed by scanning electron microscopy (SEM), and representative images of the NPs and the MPs are displayed in Figure 3A,B. Average NP and MP diameters were determined to be 140 ± 50 nm and 1.7 ± 0.9 μm, respectively. Supporting Figure S2A,B shows histogram distributions of particle sizes. TEM of the intact PLGA encapsulated 100% w/w MnO NPs and MPs shows that the MnO nanocrystals were distributed throughout both the NPs and MPs (Figure 3C,D). Total manganese content of the particles was determined using thermogravimetric analysis (TGA), and the curves for all four formulations are shown in Supporting Figure S3. As displayed in Table 1, the weight percents and the encapsulation efficiencies (EEs) of MnO for all formulations were high. One reason why EEs may be over 100% could be due to some of the polymer being washed away, while incorporating most/all of the added MnO.

Next, the MRI properties of these particles were measured at 4.0 T. Molar relaxivity, r_1 (mM^{-1} s^{-1}), is defined as the efficiency of a contrast agent to modify the relaxation rate of water protons and is governed by the equation

$$R_1 = R_{1,0} + [\text{agent}]r_1$$

where R_1 is the measured relaxation rate, $R_{1,0}$ is the relaxation rate of the solvent, and [agent] is the concentration of the agent. Intact MnO NPs and MPs had very low r_1 of 0.21 and 0.54 mM^{-1} s^{-1}, respectively. This is due to the lack of direct contact water molecules have with the nanocrystals themselves, as the nanocrystals are both hydrophobic in nature and likely still capped with oleic acid. To assess the dissolution characteristics of the particles in solution, a controlled release experiment was performed. Particles were incubated at 37 °C in either phosphate buffered saline (PBS) pH 7.4 or 20 mM citrate buffer pH 5. The two different conditions were chosen to imitate the extracellular space/cytoplasm (PBS) and the acidic environment of endosomes (citrate) within the cell.[18] As

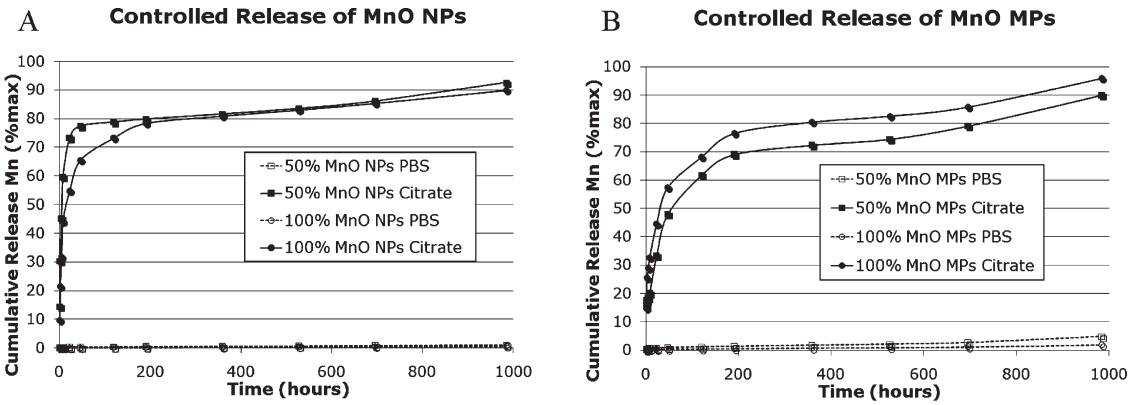

Figure 4. Controlled release of MnO (A) NPs and (B) MPs in PBS pH 7.4 (dashed lines) and 20 mM citrate pH 5 (solid lines). Cumulative release of Mn^{2+} is shown as % release over time in hours. The total duration of the study was 41 days. Note the significant release of Mn^{2+} from particles incubated in citrate buffer. The 50% w/w MnO formulations are denoted by square data points, while the 100% w/w MnO formulations are denoted by circular data points.

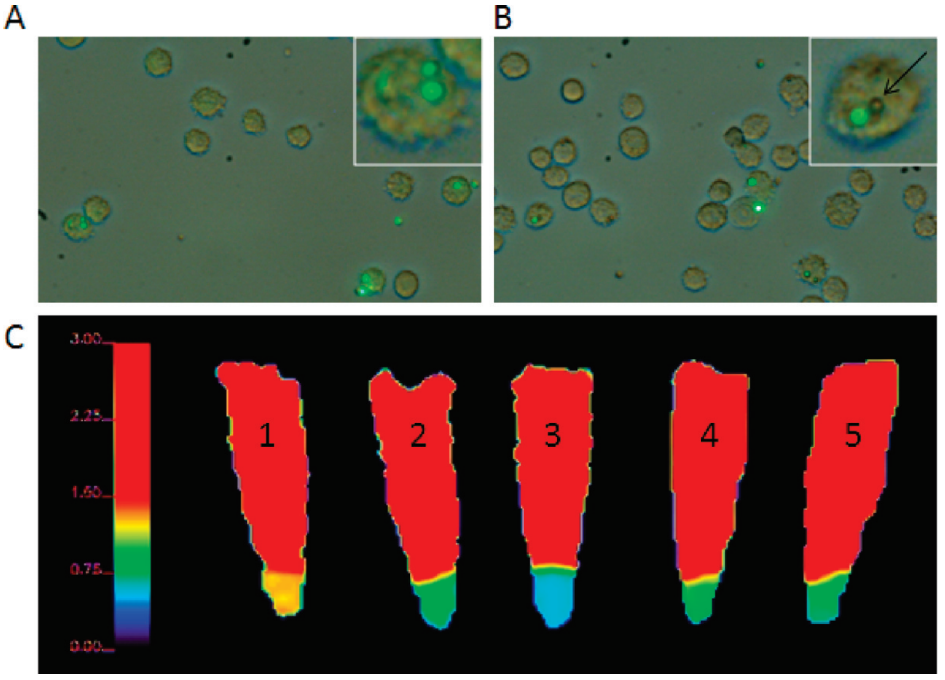

Figure 5. Bright-field and fluorescence microscopy of RG2 cells labeled with (A) 50% MnO MPs and (B) 100% MnO MPs. The green fluorescence is from the coumarin-6 inside the particles and is overlaid with the light microscopy image of the cells. Some of the MPs did not have robust fluorescence but are still visible by the light microscopy image to be inside RG2 cells (a representative MP is indicated by a black arrow). (C) T_1 maps of control and labeled RG2 cell pellets. From left to right: (1) unlabeled RG2 cells, (2) 50% MnO NPs, (3) 100% MnO NPs, (4) 50% MnO MPs, and (5) 100% MnO MPs. The scaling of the T_1 map is maximized at 1.50 s to enhance the differences of the particle-labeled cells.

discussed previously, it is well-known that particles are shuttled to endosomes following cell uptake.[17] As shown in Figure 4, particles in the citrate buffer pH 5 showed significant release of Mn^{2+} over 41 days, whereas particles incubated in PBS pH 7.4 did not. In addition, the release of Mn^{2+} from NPs was faster than MPs, as evidenced by the difference in steepness of the controlled release curves.

To study dissolution of particles within cells, MnO NPs and MPs were incubated with RG2 cells (a glioblastoma tumor cell line) for 24 h and evaluated for labeling and evolved T_1 MRI contrast. Control cells received only tumor medium. To enable particle visualization by fluorescence microscopy, coumarin-6, a green fluorescent dye, was included in particle formulations at the same time as the MnO. After 24 h, both NPs and MPs had successfully labeled RG2 cells with green fluorescence. Figure 5A,B displays the overlay of the bright-field images of the RG2 cell boundaries with the fluorescence from the MPs. The green fluorescence of the MPs can be seen in some cells in both the 50% w/w (5A) and 100% w/w formulations (5B). In general,

TABLE 2. T_1 and R_1 Values for Control and Labeled RG2 Cell Pellets

particle type	T_1 (s)	R_1 (s^{-1})
none	1.29	0.78
50% MnO NP	0.805	1.24
100% MnO NP	0.594	1.68
50% MnO MP	1.02	0.98
100% MnO MP	0.805	1.24

1−5 MPs were observed within cells. An estimate can be made on the mass of Mn per MP based on volume, density of MnO and PLGA, and encapsulation efficiency, yielding ~1 pg Mn per 100% MnO MP. Therefore, each cell contains 1−5 pg Mn.

Cytotoxicity studies were performed following labeling using the well-characterized MTS assay.[23] The MTS assay shows that, at the concentration used to label RG2 cells (50 μM Mn^{2+}), there is a slight statistically significant toxic effect elicited by the MnO NPs and MPs, as evidenced from the decreased viability compared to control cells without particles (Supporting Figure S4). Yet, there was a slight toxic effect from empty particles as well, so it is difficult to ascertain where the toxicity arises from. However, this *in vitro* assay, with particles incubating on cells in a static condition, does not accurately reflect the dynamic conditions *in vivo*.

For MRI, after incubation, the cells were washed, trypsinized, resuspended in PBS, and pelleted, after which T_1 maps were immediately acquired. As shown in Figure 5C, the T_1 values of all the labeled cells were reduced compared to the control. Therefore, R_1 was increased with the incubation of particles with the cells, and values are given in Table 2. In addition, the NPs exhibited greater R_1 compared to the respective formulations of the MPs. The addition of particles to cells caused an increase in R_1, in the following order: 50% MnO MP < 50% MnO NP = 100% MnO MP < 100% MnO NP. These results can be explained through the controlled release experiment, which showed that NPs released Mn^{2+} at a faster rate than MPs, due to a higher surface area to volume ratio. In addition, the 100% particle formulations contained more encapsulated MnO than the 50% formulations and were able to cumulatively release more Mn^{2+}, resulting in a larger increase in R_1.

There are two possibilities to explain the positive contrast that resulted following cell uptake of MnO particles: (1) the intact particles themselves were sufficient to cause a significant reduction in T_1, or (2) the particles dissolved and released Mn^{2+}, which in turn reduced T_1. Both phenomena are likely responsible to some extent. It is well-known that internalization of metallic NPs and MPs into cells results in endosomal accumulation. The data presented in Figure 4 show that particles incubated in citrate buffer pH 5, which mimics the acidic environment of endosomes, released Mn^{2+} compared to particles incubated in PBS pH 7.4 over the 41 day test period. Indeed, especially for the NPs, significant evolution of Mn^{2+} occurred within the first 24 h. The results indicate that MnO particles will not degrade in the extracellular space but will degrade upon internalization into cellular low pH endosomal compartments, releasing Mn^{2+} and subsequently causing positive contrast on T_1 images.

Without a histological marker for Mn^{2+}, electron paramagnetic resonance spectroscopy (EPR) was used to determine whether Mn^{2+} evolved from MnO intracellularly. Figure 6 shows EPR spectra recorded at room temperature (298 K) for (A) $MnCl_2$ (free Mn^{2+}), (B) cells alone, (C) MnO microparticles in pH 7.4 phosphate buffered saline (no free Mn^{2+}), and (D) cells incubated for 24 h with MnO microparticles. Spectra of all samples are shown in Supporting Figure S5. The spectrum of free Mn^{2+} shows the six hyperfine lines characteristic of a ^{55}Mn nucleus ($I = 5/2$). The EPR spectrum from cells alone shows no signal. The EPR spectrum of intact particles in PBS shows a very weak Mn^{2+} signal, possibly due to residual surface-associated Mn^{2+} in the preparation. However, this weak signal is also present in PBS. The EPR spectrum of the cells incubated with the MnO microparticles clearly shows a robust Mn^{2+} spectrum, indicative of the intracellular evolution of Mn^{2+}. When interpreting these results, it is crucial to understand that the EPR spectra of Mn^{2+} change based on the binding environment of Mn^{2+}. For example, Mn^{2+} that is free in solution exhibits sharp peaks as seen in the EPR spectrum for $MnCl_2$ in Figure 6A. The EPR spectrum of tightly bound Mn^{2+} can be very broad due to major changes in its zero-field splitting parameters and thus undetectable under our experimental conditions.[24]

The EPR spectra of the cells incubated for 24 h with the various MnO-based particles all exhibit sharp peaks, meaning that the Mn^{2+} is in a symmetric coordination environment and is not likely to be tightly bound in these samples. Whether there is a second tightly bound fraction or whether there is significant Mn remaining as MnO is difficult to ascertain from these studies and is the subject of continuing research. There is also the strong possibility of Mn^{2+} release during the course of the experiment, which in the case of these particles being useful as a slow Mn^{2+} release vehicle, is desirable. However, there is confidence that the MRI contrast created by these PLGA-encapsulated MnO particles inside cells is coming at least in part from the evolution of Mn^{2+}.

The agents reported here are "smart" contrast agents, having environmentally sensitive properties. The conversion of MnO in acidic environments to Mn^{2+} yielded a maximal change in r_1 of 0.21 to 7 mM^{-1} s^{-1}, or nearly 35-fold. Smart contrast agents are exciting for MRI as they have been useful for noninvasively probing

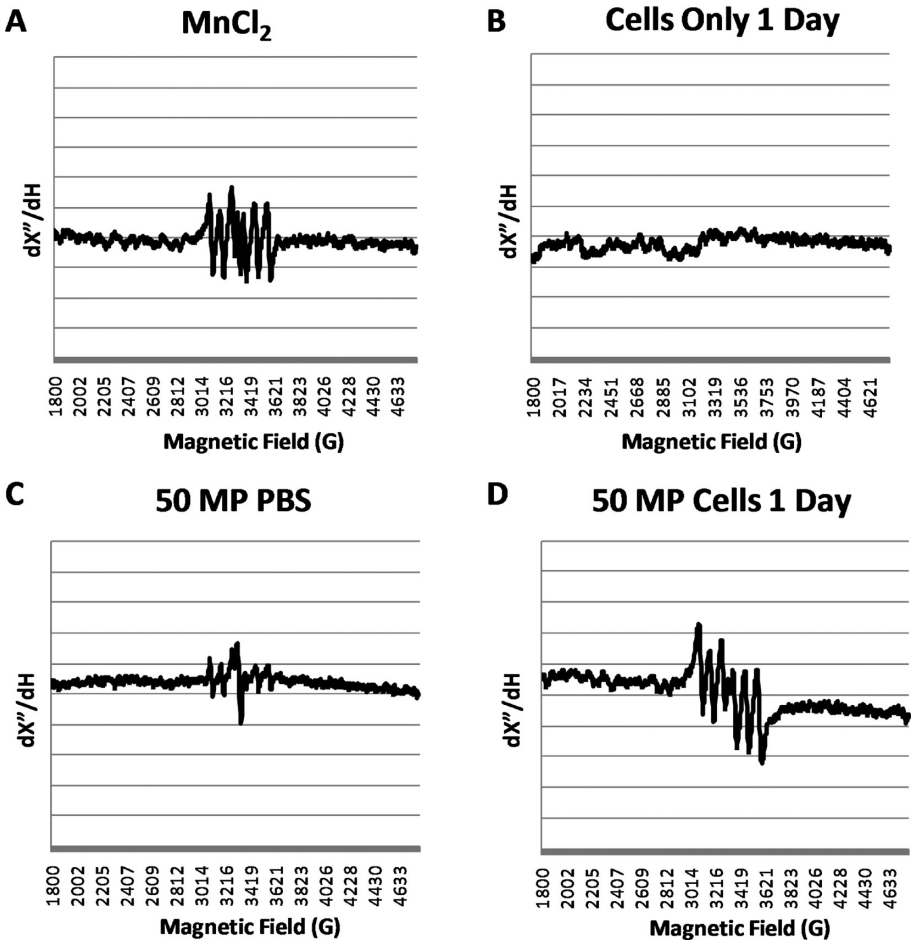

Figure 6. EPR spectra of (A) $MnCl_2$ (free Mn^{2+}), (B) cells alone, (C) 50 wt % MnO MPs in pH 7.4 phosphate buffered saline (no free Mn^{2+}), and (D) cells incubated for 24 h with 50 wt % MnO MPs.

unique biological and chemical processes within living subjects. In general, however, the dynamic range of the change in molar relaxivity of the agents in response to the biological or chemical stimulus is low. For example, EgadMe, the most recognizable smart MRI contrast agent exhibits a 3-fold increase in r_1 following enzymatic activation.[25] Various other smart contrast agents designed to sense ions similarly exhibit 2.5- to 3-fold increases in r_1.[26,27] A smart contrast agent to sense pH exhibited a maximal 2-fold increase in r_1; however, over the pH range of 7.5 to 5.5, used in our study, r_1 did not change. The change in r_1 reported in the present paper is 10-fold higher than previously reported smart contrast agents and are the most dynamic smart contrast agents ever reported.

Slow releasing Mn^{2+} formulations have several potential applications within MRI. Teslascan, a chelate of manganese and the fodipir ligand, is already clinically approved for use in visualizing liver lesions, such as tumors or hepatocellular carcinomas. The chelate is metabolized in the body and transmetalation between zinc and manganese ions occurs to release free Mn^{2+}.[28,29] The normal liver tissue preferentially takes up the Mn^{2+}, which causes bright contrast within the hepatocytes, but not within the lesions; lesions tend to not take up the contrast agent and are therefore dark on T_1 MRI images.[30,31] An alternative mechanism to slow persistent delivery of Mn^{2+} would be to use the types of particles described herein. It is well-known that following vascular administration of MPs, significant accumulation in the liver occurs, with Kupfer cell uptake being the dominant mechanism.[32] Therefore, a passive targeting mechanism to the liver is possible, with slow Mn^{2+} release.

In addition, slowly releasing MnO formulations, such as the ones described here, can be used to selectively target and visualize tumors by increasing the positive contrast of the tumor itself. Increase of the tumor signal on T_1 MRI images could result from two processes: (1) the MnO particles are taken up into the tumor cells, degraded within endosomes, and free Mn^{2+} released (2) tumors have a slightly acidic environment, ranging from pH 5.8 to 7.6 for rats and humans (median pH 7), which in itself could cause dissolution of the particles and release of the Mn^{2+}.[33] Selectivity to the tumor lesion can be achieved through the addition of ligands on the outside of the particles that target receptors, such as the folate receptor[34] or epidermal

growth factor receptor,[35] which are overexpressed on tumor cells.

Furthermore, our MnO particle formulations can be used to verify endocytosis. Particles remaining in the extracellular space will not release free Mn^{2+} and will, therefore, not elicit substantial T_1 contrast; positive contrast on T_1 images will then only be visible after internalization and dissolution of the MnO particles within endosomal compartments to release the free Mn^{2+}. This could be particularly useful for MRI experiments monitoring immune cell infiltration.[36−39] However, as with all manganese-based MRI experiments, desired manganese concentrations must be balanced by potential cytotoxicity.[16,40] Indeed, the particles formulated in this work exhibited some cytotoxicity *in vitro*, and it remains to be determined whether this *in vitro* assay is predicative for *in vivo* toxicity.

In conclusion, we have fabricated and characterized PLGA-encapsulated MnO NPs and MPs. Intact particles had low r_1. Following incubation in acidic media, the r_1 increased due to the evolution of free Mn^{2+}. T_1 values of cells incubated with particles for 24 h were decreased relative to unlabeled cells. Analyses were performed demonstrating that dissolution of the MnO to form free Mn^{2+} occurs following cell internalization into acidic endosomal compartments and likely contributes to changes in relaxation times of labeled cells.

MATERIALS AND METHODS

Synthesis of MnO Cores. Uniform 15 to 20 nm crystals of MnO were synthesized by controlled thermal decomposition of manganese(II) acetylacetonate (MnACAC) similar to the established protocol of ref 22. To generate MnO nanocrystals, 2 mmol of MnACAC was dissolved in 20 mL of benzyl ether. To this was added 2 mL of oleic acid. While stirring, the solution was then rapidly heated to 300 °C under nitrogen gas for 2 h, after which it was allowed to cool to room temperature. The nanocrystals were washed and precipitated by ethanol, collected by centrifugation at 9000 rpm for 10 min, dispersed in hexane, and dried overnight in a vacuum oven after the hexane had evaporated.

PLGA Encapsulation. A 50:50 ester-terminated PLGA, MW = 100−150 kDa with an inherent viscosity range of 0.95−1.2 dL/g, was purchased from Durect Corporation (Lactel Absorbable Polymers, Pelham, AL), and polyvinyl alcohol (PVA, MW = 12−23 kDa; 87−89% hydrolyzed) was obtained from Sigma−Aldrich (St. Louis, MO).

NPs were prepared using a single emulsion technique. One hundred milligrams of PLGA polymer was dissolved in 2 mL of methylene chloride in a glass tube. Either 50 or 100 mg of MnO dried nanocrystals was added directly to the tube of the polymer/solvent mixture, which was subsequently sonicated in a water bath and vortexed to disperse the nanocrystals. Control particles were fabricated without MnO. This organic mixture was added dropwise to 4 mL of an aqueous 5% w/v solution of PVA while vortexing at high speed. This mixture was vortexed for an additional 10 s at a high setting. The tube contents were then sonicated for 3 × 10 s at 40% amplitude with a Sonicator 350 cell disruptor (Branson Ultrasonics, Danbury, CT) to create an oil-in-water emulsion. Immediately after sonication, the emulsion was poured into 60 mL of an aqueous 0.3% w/v PVA solution, under rapid stirring with a magnetic stirrer. The resulting nanosized particles were stirred in solution for 3 h to allow for methylene chloride evaporation. The NPs were then collected by centrifugation at 12 000 rpm for 10 min, washed three times with deionized water, resuspended in deionized water, flash frozen in liquid nitrogen, and dried on a lyophilizer.

MPs were prepared similarly to NPs except for four differences: (1) The polymer/solvent/MnO nanocrystal mixture was added dropwise to 4 mL of an aqueous 1% w/v solution of PVA while vortexing at high speed. (2) This mixture was sonicated on a T10 basic ULTRA-TURRAX homogenizer (IKA, Wilmington, NC) at the power setting of 5.5 for 3 × 10 s. (3) This oil-in-water emulsion was poured into 60 mL of an aqueous solution of pure deionized water. (4) After the methylene chloride evaporation step, the MPs were collected by centrifugation at 4000 rpm for 10 min. Washing and freeze-drying was similar to that for NPs.

Fluorescent MnO NPs and MPs were fabricated by adding 500 μL of a 2 mg/mL methylene chloride solution of coumarin-6, a green fluorescent dye, to all formulations at the same time as the MnO nanocrystals were added to the polymer/solvent mixture.

Physical Characterization of Cores and Particles. MnO nanocrystals and intact particles were characterized immediately after synthesis. Powder X-ray diffraction (XRD) was performed on ∼100 mg samples of dry MnO, utilizing a Scintag PAD V diffractometer, in the Department of Geology and Geophysics, Yale University, and was used to identify crystal structure and molecular identity. Transmission electron microscopy (TEM) was performed on MnO nanocrystals and PLGA-encapsulated particles dried on carbon-coated copper grids. A Tecnai 12 Biotwin system was utilized, operating at 120 kV in the Yale Center for Cellular and Molecular Imaging, to measure the size of MnO nanocrystals and to analyze core distribution within particles. Scanning electron microscopy (SEM) images of the intact, lyophilized particles were taken on a JEOL JXA-8600 electron microprobe in the Department of Geology and Geophysics, Yale University. Average particle size was determined through post-processing of the SEM images with ImageJ. Total manganese content of the particles was investigated by thermogravimetric analysis (TGA) using the TA Instruments Q50 model (New Castle, DE).

MRI Properties of Particles. Two different MRI experiments were performed. The first was the measurement of r_1 molar relaxivities of intact MnO nano- and microparticles formulated with 100% w/w MnO. Particles were suspended in phosphate buffered saline (PBS) at pH 7.4 and subsequently suspended in equal volume of 1.0% agarose to achieve Mn^{2+} concentrations of 2.5, 1.25, 0.625, and 0.313 mM. The last tube contained only agarose and saline. Agarose was necessary to prevent sedimentation during T_1 mapping.

MRI was performed at 4.0 T on a Bruker Biospec horizontal bore spectrometer. T_1 mapping was generated by the saturation recovery method using a short TE gradient echo sequence. Ten repetition times logarithmically spaced from 25 ms to 5 s were used to acquire images of the tubes. T_1 fitting was accomplished offline using the T_1 relaxation equation, which was executed by IDL (Boulder, CO).

To measure the longitudinal MRI properties of particles, NPs and MPs were resuspended in two different solutions. The first solution was PBS pH 7.4, mimicking the extracellular pH in tissue and intracellular cytosolic pH. The second solution was 20 mM sodium citrate at pH 5, mimicking the acidic intracellular environment of endosomes.[18]

Ten milligrams each of 50% w/w and 100% w/w NPs and MPs were placed into separate 1.5 mL plastic vials, suspended in 1 mL of either the PBS or citrate buffer solution, and incubated with continual 360° inversion in a cell culture incubator at 37 °C. At desired time points, the plastic vials were microcentrifuged at

10 000 rpm for 10 min to pellet the particles and the supernatants transferred to other plastic vials for subsequent MRI. At each time point, 1 mL of fresh PBS or citrate buffer was added to the pelleted particles, followed by resuspension and incubation. The following time points were used: 1 h, 2 h, 5 h, 8 h, 1 day, 2 days, 5 days, 8 days, 15 days, 22 days, 29 days, and 41 days post-mixing particles in the solutions. MRI was performed on retrieved supernatants as described above, except without agarose. Mn^{2+} concentrations were calculated from the T_1 values using a measured r_1 for Mn^{2+} of 7 mM^{-1} s^{-1}.

Cell Labeling and MRI. Rat RG2 glioma cells (American Type Culture Collection, Manassas, VA) were cultured in high glucose DMEM, supplemented with 10% FBS and 1% penicillin streptomycin. To evaluate the ability of the NPs and MPs to label cells, 20 μL of 5 mg/mL coumarin-6-doped, fluorescent MnO NP and MP solutions in media were added to confluent culture dishes of rat RG2 cells and allowed to incubate for 24 h. Cells were then washed to remove free particles three times in PBS, trypsinized, and centrifuged at 1000 rpm for 5 min. The cell pellet was resuspended in PBS; cells were pipetted onto a slide, coverslipped, and immediately examined on a Leica MZ16FA stereo motorized fluorescence microscope, equipped with a Leica DFC300 FX camera (Leica Microsystems, Cambridge, UK). To analyze whether particles were endocytosed, dual bright-field and green fluorescent photomicrographs were acquired. More than 50 cells were analyzed to determine the range of internalized particles per cell.

To investigate the ability of cells to endocytose particles and then dissolve the MnO nanocrystals, the same amounts of nonfluorescent MnO NPs and MPs were added to confluent RG2 cells and incubated for 24 h. Control cells received only the tumor culture medium. The cells were processed as above except that the resulting cell pellets were resuspended in PBS and transferred to 0.5 mL plastic vials. The vials were spun on a microcentrifuge at 2000 rpm for 3 min to pellet the cells. Cell tubes then underwent T_1 mapping as above, and both T_1 and R_1 values for the cell pellets were determined.

EPR Measurements. All EPR spectra were recorded at room temperature (298 K) on a Bruker ELEXYS E500 EPR spectrometer. Experimental parameters: 9.4 GHz microwave frequency, 1 mW power, and 30 G modulation amplitude. Each sample was loaded onto a 10 μL capillary tube, which was then sealed with clay and placed in an EPR tube (4 mm o.d.) to record the spectrum.

Cytotoxicity. An MTS assay (CellTiter 96 AQueous One Solution Cell Proliferation Assay, Promega, Madison, WI) was performed to assess cell cytotoxicity after NP and MP exposure. Briefly, 1×10^4 RG2 cells were added to wells in a 96-well plate and grown to 70% confluency. Then, various concentrations of MnO PLGA NPs and MPs, as well as blank PLGA NPs and MPs, were added to the cells and incubated at 37 °C. Control wells had just fresh tumor medium added to the cells. After 48 h, cells were washed with RG2 medium and then 100 μL of fresh medium was added to each well, followed by 20 μL of the MTS reagent. The plate was incubated for 3.5 h at 37 °C. Viability was quantified using a microplate reader at absorbance wavelengths of 490 and 700 nm (700 nm was used as reference). Percent viability was calculated by dividing the absorbance value for each sample well by the average absorbance value of the control wells, multiplied by 100. All samples were assayed in quadruplicate.

Acknowledgment. This work was supported by NIH Grants DP2 OD004362 and P30 NS052519.

Supporting Information Available: X-ray diffraction of MnO cores, histogram analysis of nano- and microparticle diameters, TGA traces of polymer-encapsulated MnO nanocrystals, cytotoxicity data, and EPR spectra. This material is available free of charge *via* the Internet at http://pubs.acs.org.

REFERENCES AND NOTES

1. Lauterbur, P. C. Progress in NMR. Zeugmatography Imaging. *Philos. Trans. R. Soc. London, Ser. B* **1980**, *289*, 483–487.
2. Lee, J. H.; Silva, A. C.; Merkle, H.; Koretsky, A. P. Manganese-Enhanced Magnetic Resonance Imaging of Mouse Brain After Systemic Administration of MnCl2: Dose-Dependent and Temporal Evolution of T1 Contrast. *Magn. Reson. Med.* **2005**, *53*, 640–648.
3. Tambalo, S.; Daducci, A.; Fiorini, S.; Boschi, F.; Mariani, M.; Marinone, M.; Sbarbati, A.; Marzola, P. Experimental Protocol for Activation-Induced Manganese-Enhanced MRI (AIM-MRI) Based on Quantitative Determination of Mn Content in Rat Brain by Fast T1Mapping. *Magn. Reson. Med.* **2009**, *62*, 1080–1084.
4. Angenstein, F.; Niessen, H. G.; Goldschmidt, J.; Lison, H.; Altrock, W. D.; Gundelfinger, E. D.; Scheich, H. Manganese-Enhanced MRI Reveals Structural and Functional Changes in the Cortex of Bassoon Mutant Mice. *Cereb. Cortex* **2007**, *17*, 28–36.
5. Tucciarone, J.; Chuang, K. H.; Dodd, S. J.; Silva, A.; Pelled, G.; Koretsky, A. P. Layer Specific Tracing of Corticocortical and Thalamocortical Connectivity in the Rodent Using Manganese Enhanced MRI. *Neuroimage* **2009**, *44*, 923–931.
6. Pautler, R. G.; Silva, A. C.; Koretsky, A. P. *In Vivo* Neuronal Tract Tracing Using Manganese-Enhanced Magnetic Resonance Imaging. *Magn. Reson. Med.* **1998**, *40*, 740–748.
7. Matsuda, K.; Wang, H. X.; Suo, C.; McCombe, D.; Horne, M. K.; Morrison, W. A.; Egan, G. F. Retrograde Axonal Tracing Using Manganese Enhanced Magnetic Resonance Imaging. *Neuroimage* **2010**, *50*, 366–374.
8. Lee, J. H.; Koretsky, A. P. Manganese Enhanced Magnetic Resonance Imaging. *Curr. Pharm. Biotechnol.* **2004**, *5*, 529–537.
9. Aoki, I.; Tanaka, C.; Takegami, T.; Ebisu, T.; Umeda, M.; Fukunaga, M.; Fukuda, K.; Silva, A. C.; Koretsky, A. P.; Naruse, S. Dynamic Activity-Induced Manganese-Dependent Contrast Magnetic Resonance Imaging (DAIM MRI). *Magn. Reson. Med.* **2002**, *48*, 927–933.
10. Silva, A. C.; Lee, J. H.; Aoki, I.; Koretsky, A. P. Manganese-Enhanced Magnetic Resonance Imaging (MEMRI): Methodological and Practical Considerations. *NMR Biomed.* **2004**, *17*, 532–543.
11. Shapiro, E. M.; Koretsky, A. P. Convertible Manganese Contrast for Molecular and Cellular MRI. *Magn. Reson. Med.* **2008**, *60*, 265–269.
12. Gilad, A. A.; Walczak, P.; McMahon, M. T.; Na, H. B.; Lee, J. H.; An, K.; Hyeon, T.; van Zijl, P. C.; Bulte, J. W. MR Tracking of Transplanted Cells With "Positive Contrast" Using Manganese Oxide Nanoparticles. *Magn. Reson. Med.* **2008**, *60*, 1–7.
13. Pan, D.; Senpan, A.; Caruthers, S. D.; Williams, T. A.; Scott, M. J.; Gaffney, P. J.; Wickline, S. A.; Lanza, G. M. Sensitive and Efficient Detection of Thrombus with Fibrin-Specific Manganese Nanocolloids. *Chem. Commun.* **2009**, 3234–3236.
14. Shin, J.; Anisur, R. M.; Ko, M. K.; Im, G. H.; Lee, J. H.; Lee, I. S. Hollow Manganese Oxide Nanoparticles as Multifunctional Agents for Magnetic Resonance Imaging and Drug Delivery. *Angew. Chem., Int. Ed.* **2009**, *48*, 321–324.
15. Huang, C. C.; Khu, N. H.; Yeh, C. S. The Characteristics of Sub 10 Nm Manganese Oxide T1 Contrast Agents of Different Nanostructured Morphologies. *Biomaterials* **2010**, *31*, 4073–4078.
16. Choi, J. Y.; Lee, S. H.; Na, H. B.; An, K.; Hyeon, T.; Seo, T. S. *In Vitro* Cytotoxicity Screening of Water-Dispersible Metal Oxide Nanoparticles in Human Cell Lines. *Bioprocess. Biosyst. Eng.* **2010**, *33*, 21–30.
17. Hinds, K. A.; Hill, J. M.; Shapiro, E. M.; Laukkanen, M. O.; Silva, A. C.; Combs, C. A.; Varney, T. R.; Balaban, R. S.; Koretsky, A. P.; Dunbar, C. E. Highly Efficient Endosomal Labeling of Progenitor and Stem Cells with Large Magnetic Particles Allows Magnetic Resonance Imaging of Single Cells. *Blood* **2003**, *102*, 867–872.
18. Arbab, A. S.; Wilson, L. B.; Ashari, P.; Jordan, E. K.; Lewis, B. K.; Frank, J. A. A Model of Lysosomal Metabolism of Dextran Coated Superparamagnetic Iron Oxide (SPIO) Nanoparticles: Implications for Cellular Magnetic Resonance Imaging. *NMR Biomed.* **2005**, *18*, 383–389.

19. Bulte, J. W.; Duncan, I. D.; Frank, J. A. *In Vivo* Magnetic Resonance Tracking of Magnetically Labeled Cells After Transplantation. *J. Cereb. Blood Flow Metab.* **2002**, *22*, 899–907.
20. Shapiro, E. M.; Skrtic, S.; Koretsky, A. P. Sizing It Up: Cellular MRI Using Micron-Sized Iron Oxide Particles. *Magn. Reson. Med.* **2005**, *53*, 329–338.
21. Shapiro, E. M.; Gonzalez-Perez, O.; Garcia-Verdugo, J. M.; Alvarez-Buylla, A.; Koretsky, A. P. Magnetic Resonance Imaging of the Migration of Neuronal Precursors Generated in the Adult Rodent Brain. *Neuroimage* **2006**, *32*, 1150–1157.
22. Yin, M.; O'Brien, S. Synthesis of Monodisperse Nanocrystals of Manganese Oxides. *J. Am. Chem. Soc.* **2003**, *125*, 10180–10181.
23. Borenfreund, E.; Babich, H.; Martin-Alguacil, N. Comparisons of Two *In Vitro* Cytotoxicity Assays: The Neutral Red (NR) and Tetrazolium MTT Tests. *Toxicol. In Vitro* **1988**, *2*, 1–6.
24. Reed, G. H.; Ray, W. J., Jr. Electron Paramagnetic Resonance Studies of Manganese(II) Coordination in the Phosphoglucomutase System. *Biochemistry* **1971**, *10*, 3190–3197.
25. Louie, A. Y.; Huber, M. M.; Ahrens, E. T.; Rothbacher, U.; Moats, R.; Jacobs, R. E.; Fraser, S. E.; Meade, T. J. *In Vivo* Visualization of Gene Expression Using Magnetic Resonance Imaging. *Nat. Biotechnol.* **2000**, *18*, 321–325.
26. Li, W. H.; Parigi, G.; Fragai, M.; Luchinat, C.; Meade, T. J. Mechanistic Studies of a Calcium-Dependent MRI Contrast Agent. *Inorg. Chem.* **2002**, *41*, 4018–4024.
27. Major, J. L.; Parigi, G.; Luchinat, C.; Meade, T. J. The Synthesis and *In Vitro* Testing of a Zinc-Activated MRI Contrast Agent. *Proc. Natl. Acad. Sci. U.S.A.* **2007**, *104*, 13881–13886.
28. Toft, K. G.; Hustvedt, S. O.; Grant, D.; Martinsen, I.; Gordon, P. B.; Friisk, G. A.; Korsmo, A. J.; Skotland, T. Metabolism and Pharmacokinetics of MnDPDP in Man. *Acta Radiologica* **1997**, *38*, 677–689.
29. Schmidt, P. P.; Toft, K. G.; Skotland, T.; Andersson, K. K. Stability and Transmetallation of the Magnetic Resonance Contrast Agent MnDPDP Measured by EPR. *J. Biol. Inorg. Chem.* **2002**, *7*, 241–248.
30. Martin, D. R.; Semelka, R. C.; Chung, J. J.; Balci, N. C.; Wilber, K. Sequential Use of Gadolinium Chelate and Mangafodipir Trisodium for the Assessment of Focal Liver Lesions: Initial Observations. *Magn. Reson. Imaging* **2000**, *18*, 955–963.
31. King, L. J.; Burkill, G. J. C.; Scurr, E. D.; Vlavianos, P.; Murray-Lyons, I.; Healy, J. C. MnDPDP Enhanced Magnetic Resonance Imaging of Focal Liver Lesions. *Clin. Radiol.* **2002**, *57*, 1047–1057.
32. Shapiro, E. M.; Sharer, K.; Skrtic, S.; Koretsky, A. P. *In Vivo* Detection of Single Cells by MRI. *Magn. Reson. Med.* **2006**, *55*, 242–249.
33. Tannock, I. F.; Rotin, D. Acid pH in Tumors and Its Potential for Therapeutic Exploitation. *Cancer Res.* **1989**, *49*, 4373–4384.
34. Kamaly, N.; Kalber, T.; Thanou, M.; Bell, J. D.; Miller, A. D. Folate Receptor Targeted Bimodal Liposomes for Tumor Magnetic Resonance Imaging. *Bioconjugate Chem.* **2009**, *20*, 648–655.
35. Mamot, C.; Rochlitz, C. Targeting the Epidermal Growth Factor Receptor (EGFR)—A New Therapeutic Option in Oncology?. *Swiss Med. Wkly.* **2006**, *136*, 4–12.
36. Pirko, I.; Ciric, B.; Johnson, A. J.; Gamez, J.; Rodriguez, M.; Macura, S. Magnetic Resonance Imaging of Immune Cells in Inflammation of Central Nervous System. *Croat. Med. J.* **2003**, *44*, 463–468.
37. Hu, D. E.; Kettunen, M. I.; Brindle, K. M. Monitoring T-Lymphocyte Trafficking in Tumors Undergoing Immune Rejection. *Magn. Reson. Med.* **2005**, *54*, 1473–1479.
38. Ahrens, E. T.; Flores, R.; Xu, H.; Morel, P. A. *In Vivo* Imaging Platform for Tracking Immunotherapeutic Cells. *Nat. Biotechnol.* **2005**, *23*, 983–987.
39. Wu, Y. L.; Ye, Q.; Foley, L. M.; Hitchens, T. K.; Sato, K.; Williams, J. B.; Ho, C. *In Situ* Labeling of Immune Cells with Iron Oxide Particles: An Approach To Detect Organ Rejection by Cellular MRI. *Proc. Natl. Acad. Sci. U.S.A.* **2006**, *103*, 1852–1857.
40. Aoki, I.; Takahashi, Y.; Chuang, K. H.; Silva, A. C.; Igarashi, T.; Tanaka, C.; Childs, R. W.; Koretsky, A. P. Cell Labeling for Magnetic Resonance Imaging with the T1 Agent Manganese Chloride. *NMR Biomed.* **2006**, *19*, 50–59.